

Force characterization and commutation of planar linear motors

Arthur E. Quaid, Yangsheng Xu, and Ralph L. Hollis

The Robotics Institute
Carnegie Mellon University

Abstract

This work examines force modeling and software-based commutation for closed-loop control of planar linear motors, motivated by the need for a robust and versatile planar robot for precision assembly. The approach taken is to make measurements of the static and dynamic force capabilities of the motor as directly as possible, and determine the applicability of simple models commonly used. Measurements of force ripple, linearity with current, force reduction with skew angle, and eddy current damping forces are presented. The high-frequency current changes required for high-speed motion are shown to make the system sensitive to both the latency and update rate of the commutator and to limit the force generation capabilities at high velocities. Although this effect is caused by multiple sources, it is shown that it is well modeled as a scalar with units of time.

1 Introduction

In the Microdynamic Systems Laboratory¹ at Carnegie Mellon University, we are interested in the use of planar linear motors as components in a modular *minifactory* assembly system [1]. Planar linear motors fit into such a system by providing both coarse and fine motion capabilities in a device with a single moving part. In the minifactory, multiple planar linear motors fill the role of *couriers* carrying sub-assemblies between processing units mounted on bridges above a common tabletop workspace.

Planar linear motors consist of a moving *forcer* that can translate in two directions on a passive steel platen stator surface etched with a waffle-iron type pattern. The forcers fly on a 15 μm air bearing pre-loaded by permanent magnets, and require a tether to supply air and power. These forcers and platens are available commercially both as separate components and integrated into assembly workcells.

The particular forcer examined in this paper is shown in Fig. 1. Two sets of two *motors*² mounted orthogonally generate balanced forces about the center of mass. Each of the four motors consists of a stack of laminations and two coils, shown schematically in Fig. 2. The motors operate on a flux-steering principle, with the coil currents acting to switch the permanent magnetic flux from one set of poles to the other. The

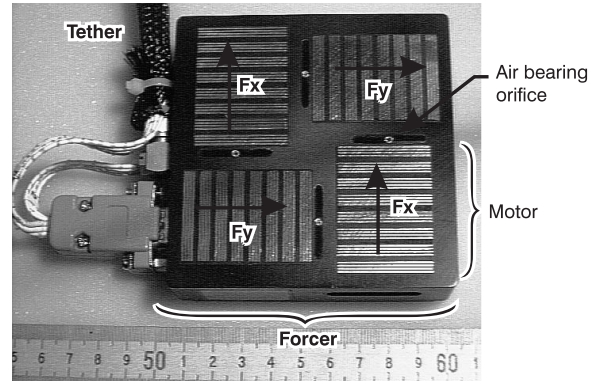


Figure 1: The underside of the Normag 4XY1302-2 planar linear motor, with 1.016 mm tooth pitch, 26 N nominal static force, 1.8 Kg mass (including interferometer optics, not shown), and 2 A operating current.

poles with the most flux tend to align themselves with the platen teeth, so that by activating the poles in the proper order, a stepping motion is achieved. The coil currents can also be *microstepped* by applying a sine wave to one coil and a cosine wave to the other. Refer to [2] or [3] for more detailed presentations of open-loop planar linear motor operation.

Although these motors have found some success in industry, their open-loop operation does not give the robustness and versatility needed for use in a minifactory. For example, as commanded speeds are increased, the motor will begin to lose synchrony and stall. In addition, open-loop operation can not provide sufficient rejection of disturbance torques during assembly operations. Closed-loop control can solve these problems, but has not yet been widely successful³ because of the lack of a suitable position sensor.

Our group is actively developing sensors that will be incorporated into the forcer for sensing platen teeth to a resolution of 1 μm . We are exploring both optical and magnetic sensing schemes [4], and have fabricated a compact 3-DOF magnetic sensor. Crawford and other students of Youcef-Toumi [5] and Ish-Shalom [6] have both independently fabricated and tested magnetic platen sensors.

The work presented in this paper makes use of a 2-DOF (translation and skew angle) high-speed laser

¹<http://www.cs.cmu.edu/~msl>

²Here, *motor* refers to one of the four actuators on the forcer, and *planar linear motor* refers to the entire device.

³The exception is the common use of accelerometers[3] to damp vibrations at high speeds and at the end of motions.

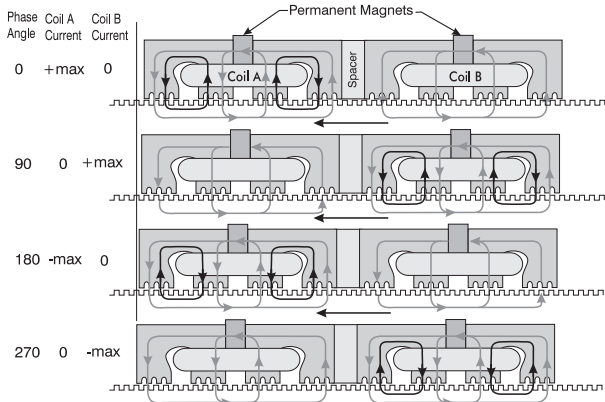


Figure 2: Basic linear motor operation: Current in the motor coils generates magnetic flux (dark flux path) that sums with the permanent magnet flux (light flux path) to produce forces.

interferometer as a position sensor. Whereas this sensor has better bandwidth and precision than a platen tooth sensor, the work presented in this paper is independent of the particular sensor used, provided it meets the minimum bandwidth and resolution requirements. This work is also independent of the higher level closed-loop control method used for controlling the forcer.

2 Motor Commutation

In the context of planar linear motors, a commutator is simply a mechanism that selects motor currents to achieve a desired force. The usefulness of a commutator is in providing higher level controllers with an ideal force source (within actuator limits), as opposed to a system where a current must be specified for each coil. Commutators separated from higher level controllers are especially important for planar linear motors because currents must be commanded at KHz rates. For example, to operate the planar linear motor of Fig. 1 at 1 m/s, a sine wave of nearly 1 KHz must be applied to the motor coils, calling for updates of at least 2 KHz.

Typically, the forcers are assumed to generate forces according to the relation:

$$F_{gen} = ki_a \sin(\phi) + ki_b \cos(\phi), \quad (1)$$

where F_{gen} is the total force generated by the x -axis motor pair, k is a constant with units of force over current, i_* is the current in coil $*$, and ϕ is the *phase* of the motor. The phase is defined as the position of the motor relative to the nearest tooth pitch, expressed as an angle:

$$\phi = 2\pi x/\tau, \quad (2)$$

where τ is the tooth pitch. This force expression assumes no manufacturing errors, no magnetic saturation, uniform teeth, perfect amplifiers, infinite update rates, and no rotation of the forcer. An identical equation applies to the y -axis motor pair.

It is convenient to re-parameterize the input currents according to:

$$i_a = i \cos(\psi) \quad \text{and} \quad i_b = -i \sin(\psi), \quad (3)$$

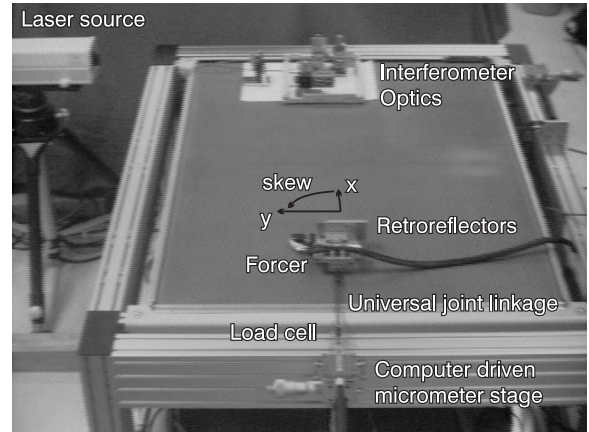


Figure 3: Test setup for static force measurements.

where i and ψ are the new parameters. Combining (1) and (3) and simplifying yields:

$$F_{gen} = ki \sin(\phi - \psi). \quad (4)$$

For open-loop control, force is not usually controlled, but rather the equilibrium position of the motor. Typically, i is kept constant at the maximum value, and a value of $\psi = \phi_{des}$ is used to shift the equilibrium position of the motor to ϕ_{des} .

For closed-loop control, a *fixed amplitude* commutator can be designed that also keeps i at its maximum value. However, ψ is now varied to generate forces by setting it to $\psi = \phi - \arcsin(F_{des}/ki)$. This commutation scheme requires large currents to be in the motor coils at all times, resulting in unwanted thermal effects, but also a potentially useful passive stiffness.

Alternatively, the other input parameter, ψ , can be fixed relative to the motor position ϕ so that the motor is always operating at the peak of the stiffness curve by setting $\psi = \phi - \pi/2$. In this approach, force is controlled by varying the amplitude i according to $i = F_{des}/k$. This *fixed phase* commutator will have reduced thermal effects, but no passive stiffness.

In the following sections, static and dynamics tests are performed to determine whether the assumptions made for (1) are valid.

3 Static Force Characterization

Static force measurements are performed using a *locked rotor* test commonly used in motor modeling. In this test, a constant set of currents is applied to the motor coils. A load is applied to the motor through a force gauge, and the force is recorded as the motor deflects from its equilibrium position. The test setup is shown in Fig. 3.

The locked rotor test is slightly more complicated for planar linear motors because their air bearings allow for 3 DOFs. An external constraint or rotation servo is required to keep the forcer from rotating. As an external constraint would be difficult to align, the y motors of the forcer are used to regulate the skew angle to zero. A PID angle controller with a *fixed-amplitude* commutator is used for skew angle regulation and passive stiffness in the (unsensed) y direction.

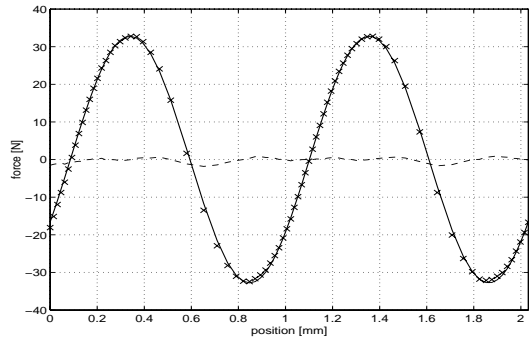


Figure 4: Force versus position (ϕ), measured data (\times) differ from a sine function (solid line) by a small error (dashed line). Here, $\psi = 0^\circ$ and $i = 2\text{A}$.

3.1 Experimental setup

The experimental setup, shown in Fig. 3, consists of a Normag forcer on a Normag platen connected through a double universal joint linkage to an Entran load cell. The load cell is mounted on a 3-axis micrometer stage, with the x translation controlled by a Newport automated micrometer. The coupling between the forcer and load cell is designed to transmit only axial forces, and to attach to the forcer as low as possible, to minimize torques that may tend to deflect the air bearing. As there is significant compliance in this coupling, a Zygo two-axis high-speed interferometer is used to monitor the true position and skew angle of the forcer.

For these tests, the currents in the x motors of the forcer are set to fixed values using (3). After setting these currents, there is a delay of 10 minutes to minimize thermal expansions during data collection. Next, the micrometer is commanded to move in short increments over a range of two pitch units. After the micrometer settles to each commanded position, the load cell and interferometer are read and the values stored. The force generated by the forcer as a function of position is shown in the stiffness curve of Fig. 4. This test is repeated with different values of parameters ψ and i in (3). The data collection procedure is fully automated, allowing more data to be collected than would otherwise be feasible.

3.2 Experimental results

A total of 127 tests were completed to generate stiffness curves for ψ from 0° to 180° , and for i from -2.0 A to 2.0 A . For each run, the micrometer was positioned every $25\ \mu\text{m}$ along a $2032\ \mu\text{m}$ (2 pitch) distance. The total data collection time was about 32 hours, taken over several days.

Fig. 4 shows a typical stiffness curve. Note that the sine function matches the data points⁴ to within 1.5 N. Also note that, neglecting higher harmonics, it is only the amplitude of the sine function which is useful, because the phase and period of the sine function are determined by the tooth pitch and the phase ϕ . Thus, only the peaks of the stiffness curves can be plotted for multiple runs on one diagram, as in Fig. 5. This figure

⁴The points are not evenly spaced due to compliance in the force linkage.

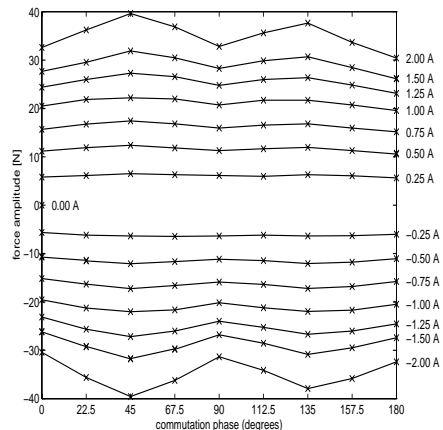


Figure 5: Force ripple, showing the peak force capability of the forcer as a function of input parameters ψ and i .

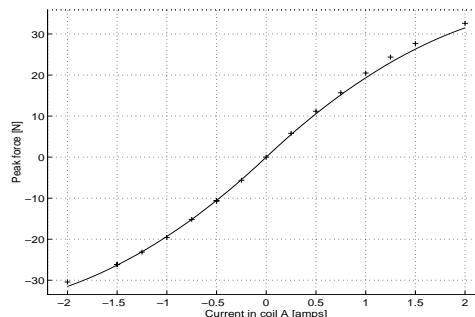


Figure 6: Force linearity, showing peak force as a function of i , with $\psi=0$. Measured values ($+$), and Eq. (5) fit to these data (solid line).

shows the variation of the peak force of the forcer as the parameters i and ψ vary.

This plot shows significant *force ripple* when the motor is commutated with (3), exceeding 20% in places. If smoother force generation is desired, these data can be used to correct the motor forces. One approach is to generate a lookup table that gives an appropriate set of currents as a function of the phase angle and desired force, as in [7]. However, this technique requires a complete set of force data to generate the lookup table for each forcer. While three days of data collection to get these data once is reasonable, it seems excessive to do this for each forcer needed in a minifactory.

Fortunately, we may be able to use a simpler technique. Plotting a vertical cross section of the data for $\psi=0$ produces Fig. 6. This curve should be close to linear if (1) is valid. However, there is significant deviation from linearity due to magnetic saturation. This nonlinear function is well modeled by a simple function such as⁵:

$$f_c = a_0 i_c - a_1 |i_c| i_c, \quad (5)$$

where i_c is the current applied to the motor coil, f_c is the peak force generated by the coil, and a_0 and a_1

⁵Chai and Leenhouts[8] have used similar empirical functions to model the saturation in rotary stepper motors.

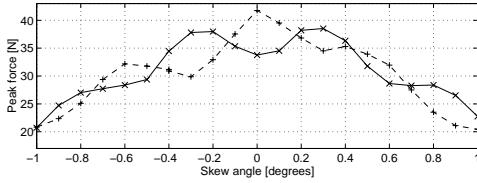


Figure 7: Peak force as a function of forcer skew angle, with $i=2$ A and $\psi_{1,2} = 0^\circ$ (solid line) or $\psi_{1,2} = 45^\circ$ (dashed line).

are positive parameters that must be determined for each motor coil. The curve connecting the data points in Fig. 6 is generated by computing the a_0 and a_1 parameters based only on the slope of the data at zero current and the magnitudes at maximum currents. In contrast to a 3D lookup table, the data needed to fit this curve can be taken in a manner of minutes using a hand-held force gauge for a *pull-out* test to determine the peak forces for only four values of i . Early results indicate that the magnetic saturation effect accounts for slightly more than half of the force ripple. The remaining ripple is probably due to higher order terms in the stiffness curves.

Force generated by the forcers is also dependent on the skew angle. As the forcer rotates slightly, the long motor teeth only partially overlap the platen teeth, causing the peak force to decrease. At large rotations, the forcers can not operate, but they can be used as a fine-motion device with a motion range of a few degrees.

To allow control of the motor skew angle, it must be included in Eq. (1). The misalignment of teeth will cause a decrease in k with increasing angle magnitude, and the phases ψ of the two motors mounted on opposite sides of the forcer will shift in opposite directions as the angle changes. Thus, Eq. (1) and Eq. (2) are replaced by:

$$F_{gen} = k(\theta)i_{a1} \sin(\phi_1) + k(\theta)i_{b1} \cos(\phi_1) + k(\theta)i_{a2} \sin(\phi_2) + k(\theta)i_{b2} \cos(\phi_2), \quad (6)$$

$$\phi_1 = \phi_x + \phi_\theta, \quad \phi_2 = \phi_x - \phi_\theta, \quad (7)$$

where ϕ_x is given by (2). The effect of θ on the phase position of each motor is reflected in the term $\phi_\theta = \theta l \cdot 2\pi/\tau$, where, θ is the forcer skew angle, and l is half the distance between each pair of motors. Note that four current values per axis are needed to control the forcer rotation, so that (3) is replaced by:

$$i_{a1} = i \cos(\psi_1 + \phi_\theta), \quad i_{b1} = -i \sin(\psi_1 + \phi_\theta),$$

$$i_{a2} = i \cos(\psi_2 - \phi_\theta), \quad i_{b2} = -i \sin(\psi_2 - \phi_\theta). \quad (8)$$

These equations will feed-forward the appropriate phase to each motor based on the rotation angle. However, the function $k(\theta)$ is still unknown. To examine this function, the locked rotor test is repeated, using the y motors to servo the forcer skew angle to non-zero values. The data in Fig. 7 show a force dropoff with increasing angle magnitude, as expected. Each plot also shows an artifact from the uncompensated force ripple, because as θ changes, the arguments of the transcendentals in (8) will change. Thus, the ripple shown as ψ varies in Fig. 5 also appears here.

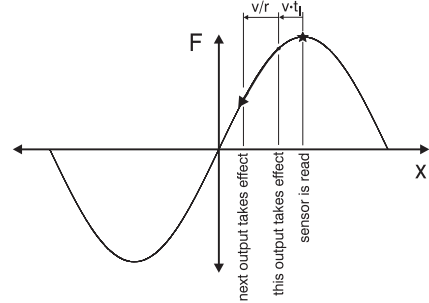


Figure 8: System latencies and control rates cause the motor's output force to drop at high velocities.

4 Dynamic measurements

The importance of dynamic effects was evident in initial closed-loop control experiments using the *fixed phase* commutator described in Sec. 2. While our open-loop controllers were able to drive motors to velocities over 1 m/s, motors under closed-loop control could not reach even half that speed. As discussed below, the reason for this limitation is delays in the commutator, which can be corrected by adding a *phase advance* term to the forcer position.

Another significant dynamic effect is the *eddy current damping* force caused by the large time-varying magnetic fields generated as the motor passes over the unlaminated steel platen surface. As these forces act in opposition to the forcer velocity, they are often treated as a mechanical damping effect [9]. As shown below, these forces can be measured by examining the acceleration responses resulting from bidirectional step force commands.

4.1 Phase advance

The initial closed-loop controller does not perform as well as the open-loop controller because the feedback loop contains delays, making the motor position sensed at the beginning of the closed-loop cycle invalid by the time the output is produced. Fig. 8 shows this effect in more detail. The stiffness curve shown assumes the motor is at the location read by the sensor. The goal is to set the motor currents so that the motor is operating at the peak of the stiffness curve, shown as a star. However, while the sensor signal is being processed and new outputs take effect, the motor will have moved, causing the output to miss the peak of the stiffness curve by an amount $v \cdot t_l$, the velocity of the motor times the latency. In addition, since the updates occur at discrete times, the motor force over the next output cycle will span a range of the stiffness curve of length v/r , where v is the motor velocity and r is the output update rate in Hz. So instead of getting the commanded force (the star), we get a reduced force that changes during the output interval (the bold arrow). By using a phase advance term of $vt_l + \frac{v}{2r}$ we can shift the bold arrow so that it is centered about the peak of the stiffness curve⁶. The approach is to determine the latency time and commutation rate of

⁶Note that the average force will always be lower than the peak for finite commutation rates, and that with fixed commutation rates, this effect will cause the available force to decrease with velocity.

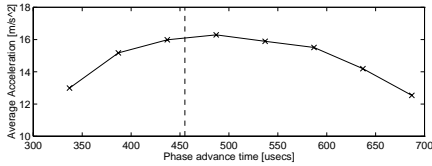


Figure 9: Average acceleration as a function of the phase advance time. The computed value is indicated by the vertical dashed line.

the commutator and compute a delay time (in units of seconds). This value is multiplied by the latest velocity to get a phase advance position offset, which is added to the latest position. The sum is the expected motor position when the output takes effect.

Commutator latencies include input and output delays and computation times. For our system, the input delay is negligible. The commutation code running on a Motorola 68040 takes $200 \mu\text{s}$ to compute output currents based on the input position.

The amplifiers introduce an output delay which is slightly more complicated to measure. To do so, a spectrum analyzer is used to measure the transfer function of the amplifier driving one motor of a stationary forcer floating on the platen. Note that the amplifier dynamics can be reasonably modeled by a constant delay time as long as the lowest frequency poles and zeros are above the driving frequencies of interest. If this is not the case, the delay time will have to vary with the commanded velocity. For our amplifier, the lowest pole appears to be at 1400 Hz, yielding a constant delay time of $114 \mu\text{s}$.

The last delay is from the commutation update rate, 3500 Hz for these tests, giving a total delay time of

$$\frac{1}{2} \cdot \frac{1}{3500} + 114 + 200 = 457 \mu\text{s}.$$

This value is the delay time that is multiplied by the motor velocity to compute the amount of phase advance.

4.2 Experimental verification

To validate the estimated phase advance delay time, full scale force commands are sent to a *fixed phase* commutator controlling the x motors of the forcer for a range of values for the phase advance delay time. As with the static force measurements, a PID controller with a *fixed amplitude* commutator controlling the y motors is used to prevent both skew angles and y translations. Force commands are generated such that the motor will accelerate forward and backwards at maximum acceleration between velocities of -1 m/s and 1 m/s several times⁷. The complete sequence typically takes less than 0.5 s, with motions of under 50 mm.

The interferometer position data for the two long constant acceleration segments are differenced to get velocity. Over repeated runs with varying phase advance delay times, the fastest response indicates the best value for the delay time. To quantify the fastest response, a velocity of 1.6 m/s is divided by the time

⁷While the forcer can move as fast as 2 m/s , the interferometer has a limit of 1 m/s .

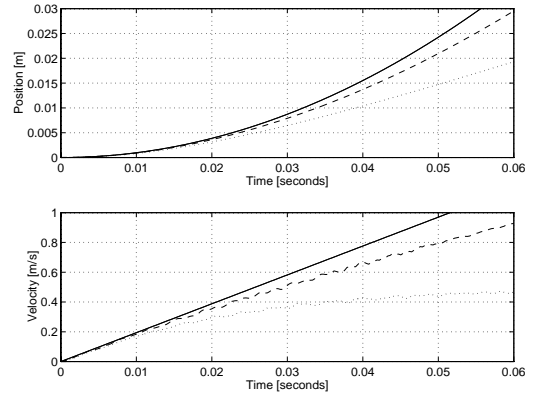


Figure 10: Trajectory (solid line) tracking with (dashed line) and without (dotted line) phase advance.

it takes for the forcer to change from $+0.8 \text{ m/s}$ to -0.8 m/s , to compute an average acceleration.

Fig. 9 shows this average acceleration as a function of the phase advance time. Note that the peak force matches the phase advance time computed in the previous section to within $50 \mu\text{s}$.

To demonstrate the improvement from the phase advance term, Fig. 10 shows the position and velocity trajectories for a peak acceleration command starting from a rest position. Note that although adding phase advance yields a substantial improvement, it is still not as fast as the theoretical maximum because of decreased forces from finite control rates and eddy current damping forces, discussed below.

It should be noted that phase advance is a common technique used in the control of stepper motors. It has even been previously applied to linear and planar motors [5, 10]. However, these works do not give much intuition on computing the phase advance functions.

4.3 Eddy current damping forces

To measure the eddy current damping force, first note that this force is always opposite in sign to the motor velocity. Thus, it increases the effective maximum actuator forces during decelerations, and decreases them during accelerations.

Using the proper value for the phase advance parameter, the bang-bang acceleration tests of the previous section are repeated. This time, the interferometer position data are differenced twice to get an acceleration signal, and filtered to reduce the noise from force ripple and other sources. The motor acceleration as a function of velocity for the two constant acceleration segments of the motor trajectory can then be plotted. The upper traces in Fig. 11 show ten repeated runs as well as an average for the positive acceleration segment of the trajectory. The lower traces show the same for the negative acceleration segment of the trajectory.

The eddy current damping force as a function of velocity is computed by averaging the upper and lower curves. This computation gives the acceleration change caused by the eddy currents, which can be multiplied by the motor mass, 1.8 Kg , to get the eddy current damping force. This result is shown in the middle trace of Fig. 11.

Although these data are rather noisy, they appear

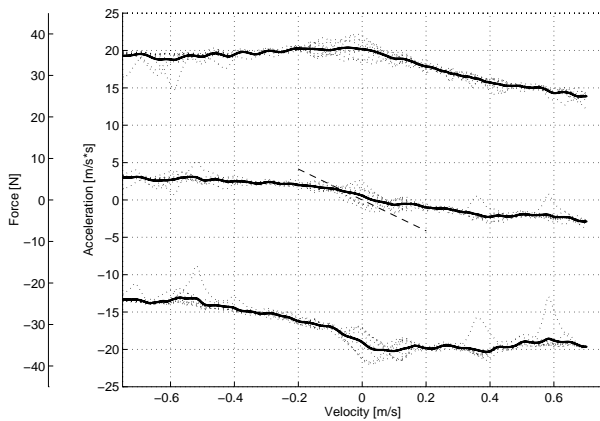


Figure 11: Acceleration and eddy current forces versus velocity. The upper and lower traces show acceleration vs. velocity. The middle trace shows the damping force. The dashed straight line is the damping force linearized about zero velocity

to show that the eddy current damping forces are not linear, but level off after a velocity of about 0.5 m/s. Ongoing work includes the use of an accelerometer and additional runs to produce a less noisy version of Fig. 11 that can be used to predict the eddy current forces at high velocities. This information is necessary to characterize the acceleration limits of the forcer for use by trajectory planners.

Nordquist and Smith [11] use an alternate method for computing the eddy current damping forces. They assume the motor can be modeled over small displacements from an equilibrium position as a linear spring-mass-damper system. An impulse response test is used to determine the damping ratio of the system based on the motor mass and local stiffness. Applying this method to the Normag forcer gives a damping coefficient, k_v , of 37.2 N/m/s. The resulting linear damping force curve from this damping coefficient is shown plotted as a dashed line in Fig. 11, which seems to match the slope of our eddy current force computation only near zero velocity. However, this estimate supports the conclusion of a non-linear eddy-current force, because if this line is extended to higher velocities, it will cause drastic drops in the available acceleration, which are not observed here.

Gjeltema [2], using a Normag motor, found the eddy current drag forces to be linear with velocity. However, only the acceleration characteristics of the motor are examined. Without deceleration data, damping forces (which *decrease* the maximum acceleration and *increase* the maximum deceleration) can not be distinguished from amplifier dynamics and commutation update rate effects (which decrease the maximum acceleration *and* deceleration).

5 Conclusions

In summary, static and dynamic force measurements of planar linear motors have been presented that support the following conclusions:

- The stiffness curve of the motor is reasonably approximated by a sine function.

- The amplitude of this sine function is a non-linear function of current.
- The available force of the forcer decreases with skew angle, falling to 50% at about $\pm 1.0^\circ$.
- A phase advance term is necessary to overcome commutator latency and update rate delay times, and can be measured by determining the time between sensor reads and output updates.
- Eddy current damping forces are non-linear and can be computed by averaging positive and negative acceleration curves at each velocity value.

This work provides the foundation for an integrated forcer/sensor under development. This platform will be used for evaluating a number of high-performance control strategies needed for application areas including precision assembly in a minifactory system.

Acknowledgements

This work is supported in part by NSF grants DMI-9523156 and DMI-9527190, and the CMU Engineering Design Research Center. Quaid is supported by an AT&T Fellowship. We thank IBM for the donation of the planar linear motor and interferometer systems, and Al Rizzi, Zack Butler, and Pat Muir for helpful discussions.

References

- [1] A. A. Rizzi, J. Gowdy, and R. L. Hollis, "Agile assembly architecture: An agent based approach to modular precision assembly systems," in *Proc. IEEE Int. Conf. Robt. Aut.*, April 1997.
- [2] P. D. Gjeltema, "The design of a closed loop linear motor system," Master's thesis, MIT, June 1993.
- [3] E. R. Pelta, "Precise positioning without geartrains," *Machine Design*, pp. 79–83, April 1987.
- [4] A. E. Brennemann and R. L. Hollis, "Magnetic and optical-fluorescence position sensing for planar linear motors," in *Proc. Int'l Conf. on Intelligent Robots and Systems*, vol. 3, pp. 101–107, August 1995.
- [5] D. S. Crawford, "Sensor design and feedback motor control for two dimensional linear motors," Master's thesis, MIT, May 1995.
- [6] J. Ish-Shalom, "Sub-micron large motion multi-robot planar motion system," in *7th ISRR Conference*, 1995.
- [7] P. F. Muir, "Converting a commercial electric direct-drive robot to operate from joint torque commands," Tech. Rep. SAND91-1548, UC-408, Sandia National Laboratories, 1991.
- [8] H. D. Chai and A. C. Leenhouts, "Position error analysis for microstepping," in *Proceedings of the Fourteenth Annual Symposium on Incremental Motion Control Systems and Devices*, pp. 265–274, 1985.
- [9] W. E. Hinds and B. Nocito, "15: The sawyer linear motor," in *Theory and Application of Step Motors* (B. Kuo, ed.), pp. 327–340, St. Paul, West Publishing Co., 1974.
- [10] J. Ish-Shalom, "Experimental results of using a step motor as a spring," in *Proc. IEEE Int'l Conf. on Robotics and Automation*, pp. 1841–1846, May 1989.
- [11] J. I. Nordquist and P. M. Smit, "A motion-control system for (linear) stepper motors," in *Proceedings of the Fourteenth Annual Symposium on Incremental Motion Control Systems and Devices*, pp. 215–231, 1985.